ELSEVIER

Physica D 144 (2000) 169–193

PHYSICA D

www.elsevier.com/locate/physd

Transport and bifurcation in a non-area-preserving two-dimensional map with applications to the discharge of pollution in an estuarine flow

J.R. Stirling

Institute for Electronic Structure and Laser, Foundation for Research and Technology, Hellas (FORTH) and Department of Physics, University of Crete, P.O. Box 2208, 71003 Heraklion, Greece

Received 2 April 1998; received in revised form 7 February 2000; accepted 10 February 2000
Communicated by J.D. Meiss

Abstract

We present an extension of the theory of transport in a fluid via lobe dynamics to the case of non-area-preserving two-dimensional maps. This extension is then applied to a two-dimensional invariant manifold occurring on a surface of a three-dimensional map of a (3+1)-dimensional flow. This flow is a time-periodic, volume preserving, cartoon of turbulent flow in an estuary. These extensions are of great use because such two-dimensional manifolds occur naturally on the bounding surfaces of three-dimensional fluid dynamical models. The study of bifurcation and transport in such models provides insight into the difficult problem of transport and pattern formation in fully coupled three-dimensional time dependent flows. We also present an application to pollution dynamics in an estuary. In particular we concentrate on the transport of material and the patchiness of clouds of pollution in such a flow.

Keywords: Chaos; Transport; Lobe dynamics; Turbulence; Pattern formation; Pollution

1. Introduction

There is a large body of work on convective mixing and transport in two-dimensional area-preserving maps (see [1–3] for an overview). There is less work, however, on the case of three-dimensional mappings [4–9] and little on dissipative two-dimensional maps (see [10,11]). This is surprising as such systems occur generically in (3+1)-dimensional fluid dynamical models. All but thin film (i.e. truly two-dimensional) flows do not preserve area on their surfaces, due to the three-dimensionality of the flow, for instance due to the effect of up-welling and down-welling. In practice, area-preserving approximations are used. However, these do not provide a good model of the transport locally. By this we mean that the elliptic fixed points of a two-dimensional area-preserving map do not model the dynamics of a patch of material being attracted into a vortex very well at all. To do this such points have to be attracting (i.e. sinks) and hence they must reside on a non-area-preserving manifold.

There are difficulties associated with these types of non-area-preserving systems as their dynamics are not so well understood. The model we present here is of a class of both the (3+1)- and (2+1)-dimensional systems, though this current work concerns a two-dimensional non-area-preserving map, which is locally dissipative. This work

E-mail address: j.r.stirling@mailcity.com (J.R. Stirling).

0167-2789/00/$ – see front matter
PII: S0167-2789(00)00054-3

is a natural extension of the standard work on chaotic advection in (2+1)-dimensional, area-preserving systems, as seen in [1–3,12–19]. This extension is important and necessary because previous work does not apply to a non-area-preserving map of a fluid flow where the unstable and stable manifolds of its saddle points do not tangle. Such behaviour is a feature of non-area-preserving or dissipative systems, which, as expressed above, can easily be shown to correspond to the free surface or any bounding surface of a fluid. We also believe that these systems will give insight into the dynamics in (3+1)-dimensional flows. It should be noted, however, that if the dynamical system is aperiodic then it is also possible to get non-tangling of the unstable and stable manifolds even for area-preserving systems. For work on aperiodic maps and flows see [20–27].

The model we present is an extension of the (3+1)-dimensional uncoupled time-periodic velocity field, proposed in [17–19], to a (3+1)-dimensional, time-periodic, fully coupled set of velocity fields. This is achieved by adding structure to the X-directional (along estuary) velocity field, to account for friction at the boundaries, and coupling it up to the Y- and Z-directional velocity fields. A stroboscopic map or Poincaré map is then taken of the flow to obtain a three-dimensional volume preserving map. The boundary conditions are such that the flow cannot pass through its bounding surfaces. This generically produces invariant manifolds on the boundaries on which the map is non-area-preserving. The model we present is of the two-dimensional time-periodic map of the flow on the ends of an estuary. We assume that no fluid leaves the estuary and hence the flow has time-periodic motion enclosed by a box, and has one free surface at the top. Therefore, unlike in [18,19], we cannot calculate an exit time for regions within the estuary. The assumption that no fluid leaves the estuary is more accurate the lower the ratio of the volume of river inflow to the flow of water in the estuary. As this ratio is low for most estuaries including the type we model, it is a reasonable assumption. As in [17–19], we assume that circulation in the vertical YZ plane is dominated by both the effects of buoyancy, and a circulation resulting from the estuary residing on a bend. The shape of the velocity fields in the other two planes is primarily a result of the effects of friction (see Fig. 1) .

We use this model to investigate the effect of the third dimension X on the dynamics of a flow. Given a certain ratio of the bend to buoyancy circulation in the YZ cross-section (to be denoted K, it should be noted that K is also approximately equal to the radius of curvature of the estuary divided by its width, see [17–19]), we investigate how the increase in the strength of interaction (α) of the X-directional component affects the global dynamics and hence the pattern formation and transport within and on the bounding surfaces of the flow. If we set $K = 11$ this would correspond to a typical value for the type of estuaries we are modeling. In this paper we deal with the bounding surfaces or ends of the estuary. In our model $X = 0$ (this corresponds to the boundary between the estuary and the river, and not half-way along the length of the estuary as in [17–19]) is always an invariant manifold with dynamics on it which are Hamiltonian. We recover the transverse circulations and velocity fields described in [17–19]. The map on the $X = 1$ sea end of our estuary is no longer Hamiltonian for $\alpha \neq 0$, and is instead usually locally dissipative. It is this map that will concern us here.

We also show the effect attracting and repelling invariant circles have on the transport within our map. We explain the implications of this in practice for fluid flows, and in particular the implications for transport and the formation of vortices in the real flow. Such structures we claim result in the creation of an important mechanism for the formation of patches of high and low concentration in clouds of pollution (see [17–19]).

As will be observed in our model, the physics of fluid mechanics, and in particular both stress free boundary conditions and rigid boundary conditions, enforce non-generic phenomena. Examples of such non-generic behaviour are non-hyperbolicity and non-transverse intersections of stable and unstable manifolds [2]. The possibility of non-transversal or even non-intersection of unstable and stable manifolds is important. This behaviour means that an extension of the theory regarding transport in a fluid via lobe dynamics to the case where there is no longer a turnstile lobe, or even a lobe, is critical to our understanding of transport in such systems.

In Section 2 we describe our model. In Section 3 we present and explain the bifurcations of the fixed points, and in Section 4 its periodic points, for a range of parameter values. Section 5 extends the transport theories of Rom-Kedar

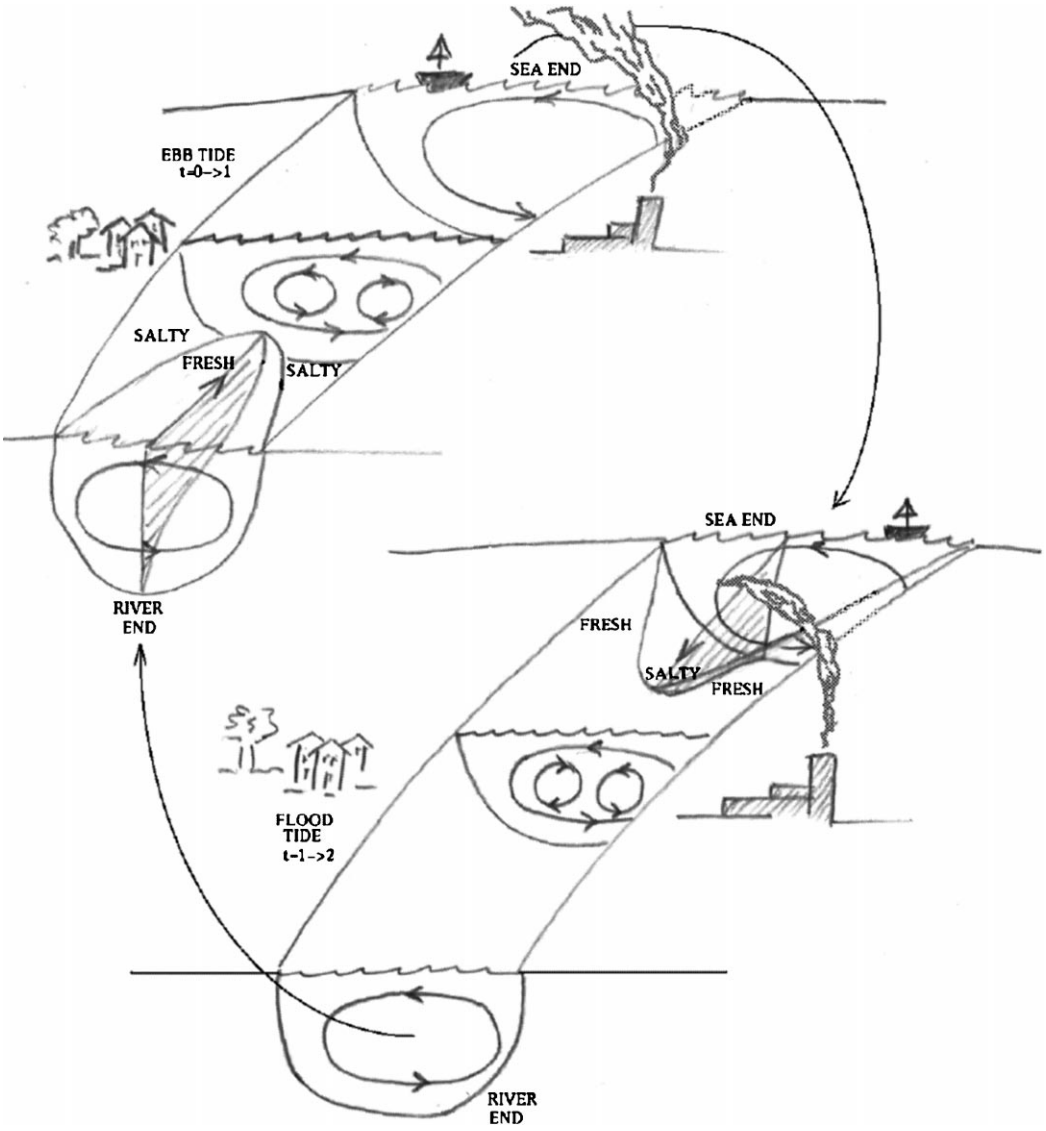

Fig. 1. Cartoon of flow in an estuary showing the single cell (wind- or bend-driven) and the periodic two cell (density driven) transverse motion.

and Wiggins [1] and Wiggins [2] (see also [17–19]), to the cases where tangling of the unstable and stable manifolds of saddle points does not occur (i.e. the tangency and post-tangency cases of a homoclinic bifurcation). We then give example applications based on our model in Section 6. Finally, in Section 7 we conclude with general comments regarding the application of such theories to dynamics on the surfaces of fluids and its implications to the dynamics of pollution.

2. A model for three-dimensional time-periodic flow in an estuary

In this section we present our modifications to the equations for the fundamental kinematic velocity fields proposed in [17–19]. The velocity fields in [17–19] include both a time-periodic buoyancy-driven circulation proposed by

Smith [28,29] (see also [30]) and verified practically by West and Mangat [31], Guymer and West [32] and Nunes and Simpson [33], and a steady bend- or wind-driven circulation (see Fig. 1). In [17–19] the velocity fields $\mathcal{V}_\mathrm{f}$ and $\mathcal{W}_\mathrm{f}$ were uncoupled with $\mathcal{U}_\mathrm{f}$, however in this paper we couple all the three velocity fields, and give some structure in the X-direction to account for the effects of boundary conditions. By this we mean we account for the effects of friction at the boundaries and also the zero velocities which occur in the X-directional velocity field when the fluid flow reverses direction on meeting the sea and river boundaries of the estuary. (This is different from the model presented in [18], as there $\mathcal{U}_\mathrm{f}$ did not necessarily go to zero at both the river and sea ends of the estuary.) We also have to ensure that volume is conserved within the system. The resulting increase in dimension obviously makes the problem no longer Hamiltonian. This (3+1)-dimensional system lies somewhere between the (2+1)- and the (4+1)-dimensional Hamiltonian cases.

Our $\mathcal{U}_\mathrm{f}$, $\mathcal{V}_\mathrm{f}$ and $\mathcal{W}_\mathrm{f}$ velocity fields, corresponding to the flow in the X, Y and Z directions, respectively, are given by

$$\mathcal{U}_\mathrm{f} = (Y^2-1)(3Y^2-1)(3Z+1)(Z+1)\alpha\{X^\beta(1-X)\}\sin(\pi t), \tag{1}$$

$$\mathcal{V}_\mathrm{f} = (3Z+1)(Z+1)(Y^2-1)[1+KY\sin(\pi t) - \alpha\{X^{(\beta-1)}(-\beta+\beta X+X)Y\sin(\pi t)\}], \tag{2}$$

$$\mathcal{W}_\mathrm{f} = Z(1+Z)^2[K(1-3Y^2)\sin(\pi t) - 2Y + \alpha\{X^{(\beta-1)}(-\beta+\beta X+X)Y^2(3Y^2-1)\sin(\pi t)\}], \tag{3}$$

which satisfy

$$\frac{\partial \mathcal{U}_\mathrm{f}}{\partial X} + \frac{\partial \mathcal{V}_\mathrm{f}}{\partial Y} + \frac{\partial \mathcal{W}_\mathrm{f}}{\partial Z} = 0. \tag{4}$$

The parameter β governs the magnitude of the circulation due to the bend, as we move along the estuary (i.e. as we change X). In all that follows we shall take $\beta = 2$. The parameter α governs the strength of the coupling between the three velocity fields. It can also be thought of as an indication of the strength of the river's X-directional velocity. Physically this means that large values of α correspond to the estuary being in flood, while small values correspond to times of drought.

Our domain is

$$0 \le X \le 1, \quad -1 \le Y \le 1, \quad -1 \le Z \le 0. \tag{5}$$

$X = 0$ defines the river end of the model, $X = 1$ the sea end. The bottom, sides and top of the estuary are defined, respectively, by $Z = -1$, $Y = \pm 1$, and $Z = 0$.

We now indicate how we derived these equations and their relationship to their Hamiltonian counterparts used in [17–19]. The brackets multiplied by α in Eqs. (1)–(3) contain the parts which make the flow non-Hamiltonian. These equations may be expressed in the form

$$\mathcal{U}_\mathrm{f} = \alpha f_1(X, Y, Z, t), \tag{6}$$

$$\mathcal{V}_\mathrm{f} = \mathcal{V}_\mathrm{f}^\mathrm{Ham}(Y, Z, t) + \alpha f_2(X, Y, Z, t), \tag{7}$$

$$\mathcal{W}_\mathrm{f} = \mathcal{W}_\mathrm{f}^\mathrm{Ham}(Y, Z, t) + \alpha f_3(X, Y, Z, t), \tag{8}$$

where

$$\mathcal{V}_\mathrm{f}^\mathrm{Ham} = \dot{Y} = (3Z+1)(Z+1)(Y^2-1)(1+KY\sin(\pi t)) = -\frac{\partial \psi_\mathrm{f}}{\partial Z}, \tag{9}$$

$$\mathcal{W}_\mathrm{f}^\mathrm{Ham} = \dot{Z} = Z(1+Z)^2((1-3Y^2)K\sin(\pi t) - 2Y) = \frac{\partial \psi_\mathrm{f}}{\partial Y} \tag{10}$$

with the stream function

$$\psi_{\mathrm{f}} = (1 - Y^2)Z(1 + Z)^2(1 + KY\sin(\pi t)), \tag{11}$$

being that used in [17–19]. Eqs. (2) and (3) can now be written as

$$\mathcal{V}_{\mathrm{f}} = \mathcal{V}_{\mathrm{f}}^{\mathrm{Ham}} - \alpha\{X^{(\beta-1)}(-\beta + \beta X + X)Y\sin(\pi t)\}(3Z + 1)(Z + 1)(Y^2 - 1), \tag{12}$$

$$\mathcal{W}_{\mathrm{f}} = \mathcal{W}_{\mathrm{f}}^{\mathrm{Ham}} + \alpha\{X^{(\beta-1)}(-\beta + \beta X + X)Y^2(3Y^2 - 1)\sin(\pi t)\}Z(1 + Z)^2. \tag{13}$$

In the above we have defined

$$f_1(X, Y, Z, t) = (Y^2 - 1)(3Y^2 - 1)(3Z + 1)(Z + 1)\{X^{\beta}(1 - X)\}\sin(\pi t), \tag{14}$$

$$f_2(X, Y, Z, t) = -\{X^{(\beta-1)}(-\beta + \beta X + X)Y\sin(\pi t)\}(3Z + 1)(Z + 1)(Y^2 - 1), \tag{15}$$

$$f_3(X, Y, Z, t) = \{X^{(\beta-1)}(-\beta + \beta X + X)Y^2(3Y^2 - 1)\sin(\pi t)\}Z(1 + Z)^2, \tag{16}$$

which satisfy

$$\alpha\frac{\partial f_2(X, Y, Z, t)}{\partial Y} + \alpha\frac{\partial f_3(X, Y, Z, t)}{\partial Z} = -\alpha\frac{\partial f_1(X, Y, Z, t)}{\partial X} = -\frac{\partial \mathcal{U}_{\mathrm{f}}}{\partial X}, \tag{17}$$

since

$$\frac{\partial \mathcal{V}_{\mathrm{f}}^{\mathrm{Ham}}}{\partial Y} + \frac{\partial \mathcal{W}_{\mathrm{f}}^{\mathrm{Ham}}}{\partial Z} = 0. \tag{18}$$

The functions f_2 and f_3 are chosen to have minimal effects on the global dynamics generated by the $\mathcal{V}_{\mathrm{f}}$ and $\mathcal{W}_{\mathrm{f}}$, respectively. By this we mean, we know what global mode of circulation we want to model in the YZ plane, and we know what shape the velocity field should be in the XY and XZ planes (see Fig. 1), therefore the additions f_2 and f_3 should have a minimal effect on these features. This results in a fully coupled set of volume preserving equations which are a kinematic cartoon of the estuarine flow. The additions f_2 and f_3 satisfy the same boundary conditions as $\mathcal{V}_{\mathrm{f}}^{\mathrm{Ham}}$ and $\mathcal{W}_{\mathrm{f}}^{\mathrm{Ham}}$, respectively.

From Eq. (1) the sea end of the model $X = 1$ can be seen to be an invariant manifold. The equations governing the dynamics on it are

$$\mathcal{U}_{\mathrm{f}} = 0, \tag{19}$$

$$\mathcal{V}_{\mathrm{f}} = (3Z + 1)(Z + 1)(Y^2 - 1)[1 + KY\sin(\pi t) - \alpha\{Y\sin(\pi t)\}], \tag{20}$$

$$\mathcal{W}_{\mathrm{f}} = Z(1 + Z)^2[K(1 - 3Y^2)\sin(\pi t) - 2Y + \alpha\{Y^2(3Y^2 - 1)\sin(\pi t)\}]. \tag{21}$$

These equations can be seen to be a non-area-preserving perturbation of the Hamiltonian case which occurs at $X = 0$ (i.e. when $X = 0, \mathcal{U}_{\mathrm{f}} = 0, \mathcal{V}_{\mathrm{f}} = \mathcal{V}_{\mathrm{f}}^{\mathrm{Ham}}$ and $\mathcal{W}_{\mathrm{f}} = \mathcal{W}_{\mathrm{f}}^{\mathrm{Ham}}$). The term α can be thought of as a parameter which models the relative magnitudes or the strength of the coupling of the along-estuary X velocity to the transversal Y and Z velocities, or in other words the strength of the perturbation. As in [17–19] the term K governs the relative strength of the bend-driven circulation to the buoyancy-driven circulation in the vertical plane. As in [17–19] we take $K = 11.0$ which is typical for the type of estuaries we model.

In the next section we consider the effect of varying the parameter α in order to see the effect on the dynamics at the sea end, $X = 1$, of an increased influence of non-area-preserving addition caused by the addition of the third dimension, X, to the Hamiltonian equations. In what follows, we shall study Eqs. (20) and (21). Despite the form of the equations we shall not, however, treat our system as a perturbation of the Hamiltonian case. This is because the values of α we are interested in, soon become too large for such a treatment. Application of Melnikov's method [2,4,10,11], and other such techniques, therefore is inappropriate for our model.

3. Bifurcation of the fixed points

In this section we begin by considering the unstable and stable manifolds of the central saddle point from $\alpha = 0$ to 10 (see Fig. 2(a)–(g)). With the use of these plots we then explain the bifurcations which are undergone by the saddle and the elliptical fixed points or foci. This does not present the whole bifurcation picture for our system, but it does give an example of the type of bifurcations occurring in the physical regime in which we are interested.

For $\alpha = 0$ we have a Hamiltonian system. We get the standard picture, see [17–19], with a saddle and two elliptical fixed points. For $\alpha \neq 0$ we have two foci, one a source and one a sink, instead of the elliptical fixed points seen

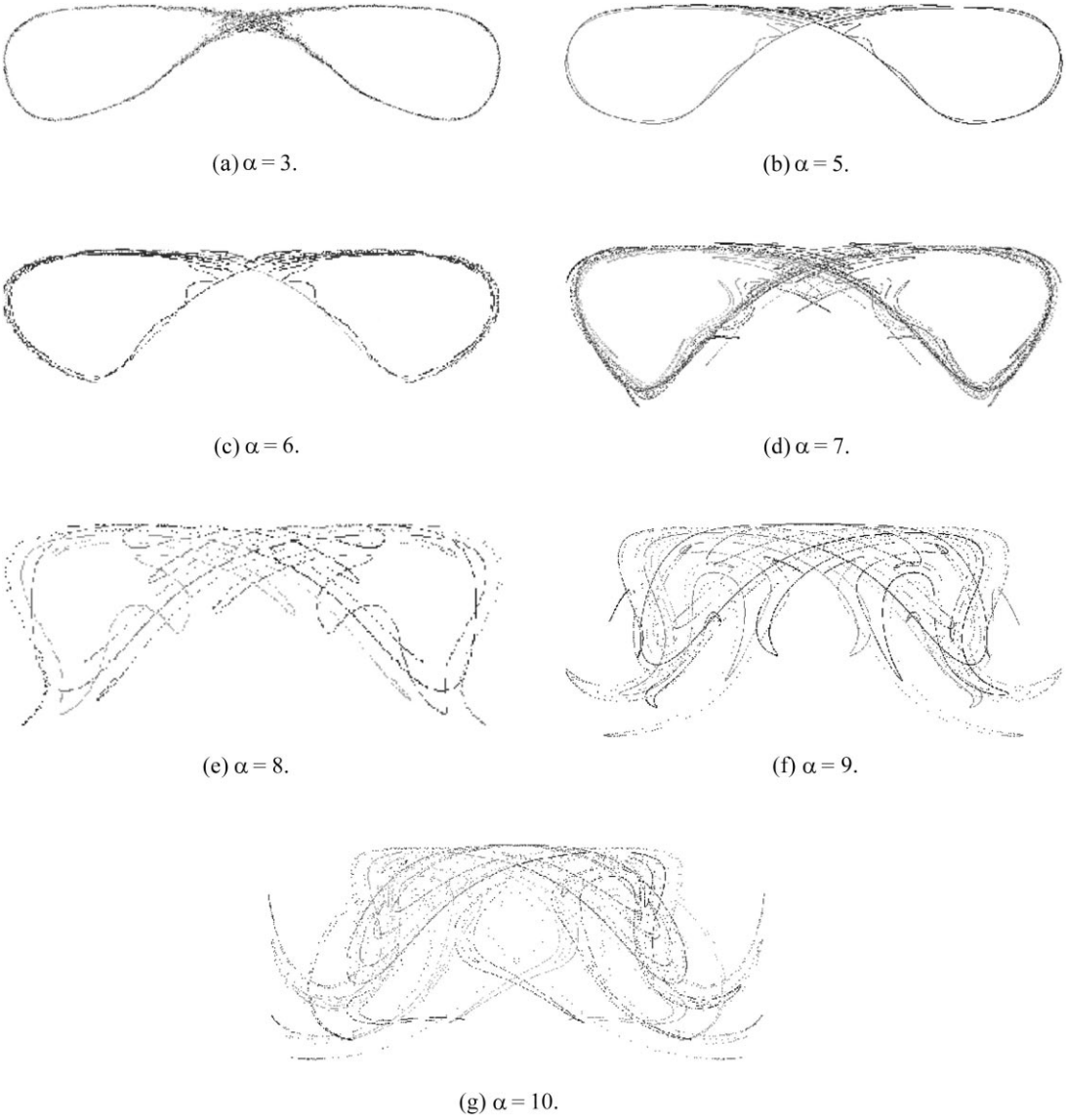

(a) $\alpha = 3$. (b) $\alpha = 5$. (c) $\alpha = 6$. (d) $\alpha = 7$. (e) $\alpha = 8$. (f) $\alpha = 9$. (g) $\alpha = 10$.

Fig. 2. The unstable and stable manifolds of the saddle fixed point $\alpha = 3$–10.

in the Hamiltonian system. As α is increased the unstable and stable manifolds of the saddle fixed point undergo a homoclinic bifurcation, as can be seen in Fig. 2(a)–(c). For low values of α we see a homoclinic tangle (Fig. 2(a)), as we increase α this goes through a homoclinic bifurcation to form a homoclinic tangency (see Fig. 2(b)). Beyond this the manifolds cease to touch (see Fig. 2(c)), further increases in α lead to a return to the tangency case and then back to a tangle (Fig. 2(d)). The lobes of the tangle then become progressively more wild with increasing α (see Fig. 2(d)–(g)). It can also be seen from these lobe diagrams (Fig. 2(d)–(g)) that the attracting and repelling fixed points in the top left- and right-hand corners of our map, respectively, increase their strength with increasing α. This can be seen by their increased effects on the dynamics of the unstable and stable manifolds of the saddle fixed point. For larger values of α (e.g. $\alpha = 9.3$) we find that the focus has undergone a period doubling bifurcation to a saddle and a period two foci chain.

As a general comment on the global dynamics, we expect to inherit some of the legacy of the Hamiltonian $\alpha = 0$ limit. Similar behaviour is observed by Arrowsmith et al. [34,35] in their investigation of the Bogdanov map. Using the experience gained from the Bogdanov map we therefore expect to get period doubling bifurcations of foci and the existence of Birkhoff periodic points for sufficiently small values of α.

3.1. Three invariant circles and their bifurcation

Associated with the saddle fixed point we have three invariant circles (see Fig. 3) for the range of parameter values, α, in which we are interested. To understand where these came from we use the bifurcation diagram (see Fig. 4) for the strong 1:2 resonance [36] (see also [37–39]. Though this results from a much simpler and somewhat different system (it is a velocity field and not necessarily the one corresponding to an approximating system for our mapping), it is useful in understanding how these invariant circles behave. This is because it shows a set of bifurcations associated with a saddle and two foci fixed points similar to those we observe numerically. As can be seen in Fig. 3 our mapping has a small attracting invariant circle associated with the homoclinic bifurcation of the unstable and stable manifolds of the saddle fixed point and the left fixed point focus. There is also a similar small invariant circle on the right-hand side of the map, this however is repelling and hence cannot be seen in the Poincaré map. On the inside of the tangle associated with the saddle fixed point we see no invariant circle for small values of α, as it is absorbed into the tangle. This is similar to, but somewhat more complicated than, the case P in the strong 1:2 resonance bifurcation diagram (see Fig. 4), where the invariant circles C_2 and C_3 are absorbed into a homoclinic

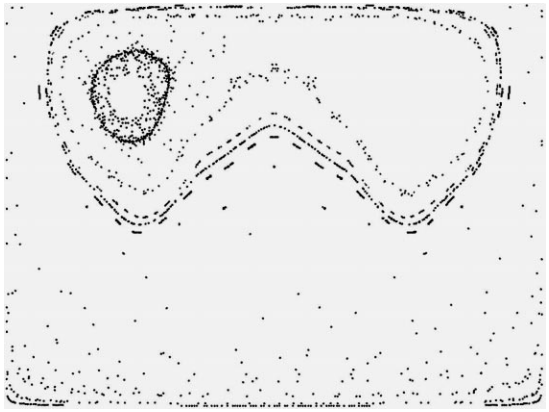

Fig. 3. The Poincaré map for $\alpha = 5.91$, showing one large and one small invariant circle. The other small invariant circle is repelling and therefore is not seen on this map.

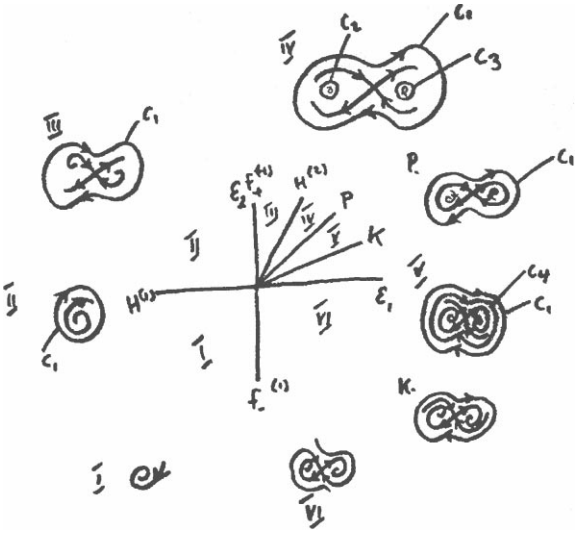

Fig. 4. The bifurcation diagram for the strong 1:2 resonance [36], showing the formation and break-up of the invariant circles C_1, C_2 and C_3.

connection of the unstable and stable manifolds of the saddle. When the tangle bifurcates to form a homoclinic tangency and then beyond we see two invariant circles on the inside, one repelling around the sink on the right-hand side of the map, and one attracting, around the source on the left-hand side (see Fig. 3). As α is increased these two invariant circles decrease in size, until they cease to exist. This is similar, though ultimately different from the case IV in the strong 1:2 resonance bifurcation diagram where the invariant circles are created from a Hopf bifurcation (see Fig. 4). Our foci then bifurcate in a period doubling bifurcation to form saddles, with two foci.

We also see one large invariant circle on the outside of the tangle. This we believe comes from another part of the parameter space, as is the case for the curve C_1 in the bifurcation diagram for the strong 1:2 resonance [36] (see Fig. 4). This invariant circle survives for a range of α and then it is destroyed by the unstable and stable manifolds of the saddle fixed point. The periodic chain seen on the outside of the tangle beside the invariant circle (see Fig. 3) is an example of the non-resonant behaviour of some of the Birkhoff periodic chains described in Section 4.

3.2. Bifurcation of an invariant circle

Linear stability analysis of the two foci reveals them to be neutral for all parameter values. Hence stability or instability is governed by the nonlinear terms. We now look at the bifurcations of the foci and the invariant circles surrounding them. Unexpected things occur if we look at the nature of the fixed point as the small invariant circle, seen in Fig. 3, appears and on until the focus undergoes a period doubling bifurcation to a saddle. All through this range of α values the stability of the focus remains the same even though an invariant circle appears and then disappears. This is important as we would expect to see a change in the sense of the focus, if the invariant circle's presence was a result of a Hopf bifurcation.

If we now look at the unstable and stable manifolds and the lobe diagrams for the hyperbolic fixed point for values of α from 8 to 10 (see Fig. 2(e)–(g)) we see that they become more and more wild with increasing α until they take up nearly all of the phase space enclosed by them. This suggests that in this part of the parameter space, these two small invariant circles are destroyed by the stable and unstable manifolds of the saddle fixed point. This would explain why we lose the invariant circle and see the focus on its own, up until the point where it bifurcates to a saddle. It does not, however, explain how the invariant circle was born. We expect that this happens due to

the invariant circle existing in a nearby part of the parameter space where the focus fixed point was elliptical. This elliptical fixed point bifurcates in a period-doubling bifurcation to a saddle, with two elliptical period-2 points, surrounded by an invariant circle. This is a generic bifurcation for Hamiltonian systems. In the dissipative case, the same bifurcations occur but the elliptical fixed points are replaced by foci around which there is an invariant circle, for a sufficiently small perturbation of the Hamiltonian case. This would account for the fact that there is no change of the sense of the focus, and also the presence of an invariant circle.

4. Resonance and the passage of an invariant circle

In this section we look more closely at the small attracting invariant circle seen around the left-hand focus in Fig. 3. We present the example of the bifurcations undergone by unstable and stable manifolds of period-4 and -5 hyperbolic orbit when the invariant circle passes through them, as we increase α. (For a more complete picture of the different possible bifurcations undergone when an invariant circle comes into and out of resonance with a period-4 orbit see, in particular [40–42]. See also [37,43].) These specific periodic orbits are used as they give a clear example of the type of bifurcations undergone generically for the periodic orbits of this system. The main objective is to show the bifurcations associated with the unstable and stable manifolds of the saddles and the interaction of these manifolds with the invariant circle. This as we shall show in the next section has important implications for transport in our model.

As the parameter α increases the rotation number of the invariant circle passes through $\frac{1}{4}$ and $\frac{1}{5}$, hence becoming resonant with period-4 and -5 orbits, respectively. Further increases see the invariant circle become resonant with a period-3 orbit, though we do not show this. We look at the interaction of the invariant circle with these periodic orbits and show a sequence of bifurcations similar to those seen in the Bogdanov map studied by Arrowsmith et al. [34,35]. It has to be remembered that this sequence is also mirrored on the opposite side of the map, though the stability of the foci and invariant circles are opposite.

The invariant circle appears (in resonance with a period-3 Birkhoff periodic orbit) for reasons discussed in the previous section, at approximately $\alpha = 8.25$. This invariant circle increases in size with decreasing α, as explained in the previous section. We expect the resulting bifurcations to be similar to those on passage between Arnold tongues. As we change the parameter α the attracting or repelling invariant circle has rational and irrational rotation numbers, hence becoming resonant with a periodic orbit or existing as an invariant circle, respectively. The non-resonant orbits are to be expected because as pointed out by Arrowsmith et al. [34,35] there is an important difference between the two-dimensional and one-dimensional maps. In one-dimensional circle maps the Arnold tongue is synonymous with resonance. In a two-dimensional map, however, the Arnold tongue can coexist with resonant behaviour occurring elsewhere in the phase space. These attractors are difficult to see numerically and are in most cases of a limited importance as they have small basins of attraction. This non-resonant phenomena can be seen in many of our Poincaré maps (see Fig. 3). If we look at the invariant circle, it continues to grow to the point when it is destroyed by the homoclinic tangle in a homoclinic bifurcation, or a so-called blue sky catastrophe [44].

We watch the passage of the invariant circle and its interaction with the Birkhoff periodic orbits with increasing α. First we see the outer unstable manifolds of the periodic saddle points converging onto the attracting invariant circle (Fig. 5(a)). As α is increased the circle comes closer to the periodic orbit, until eventually it merges into the outer unstable and stable manifolds of the saddle orbits which appear to join in a smooth heteroclinic connection (Fig. 5(b)). Further increases in α lead to the invariant circle being destroyed for an interval of α values (Fig. 5(c)). Once α is increased beyond this interval of values the inner unstable and stable manifolds of the saddles join in heteroclinic connection (Fig. 5(d)). Further increases in α find the invariant circle now on the inside of the periodic orbit and attracting the inner unstable manifolds of the periodic saddles (Fig. 5(e)). The invariant circle continues to

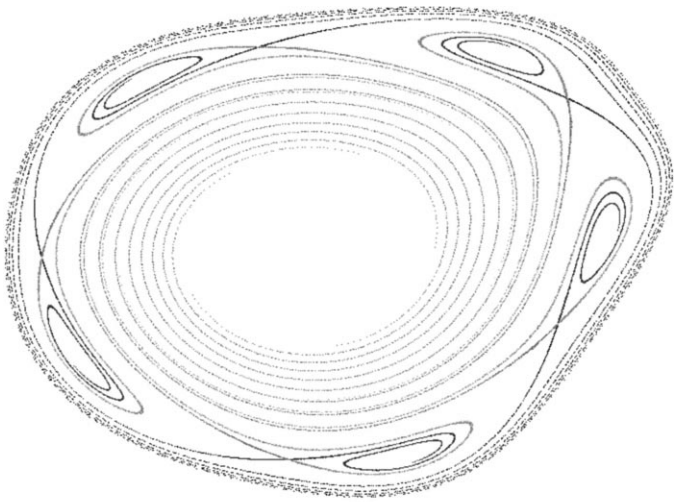

(a) $\alpha = 5.5$.

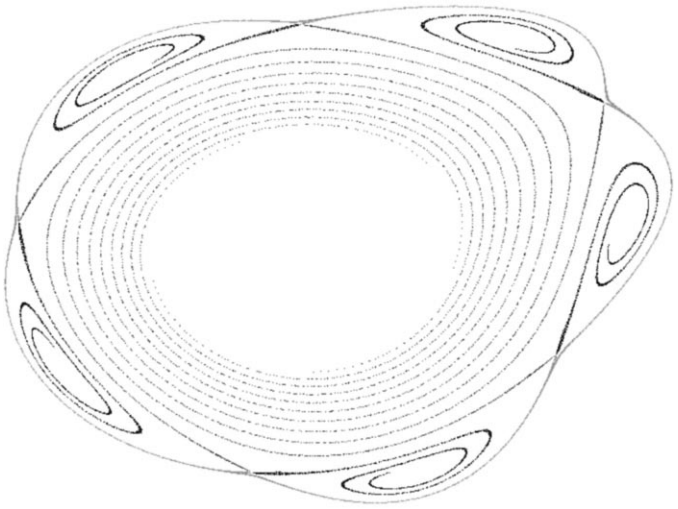

(b) $\alpha = 5.587$.

Fig. 5. The phase portrait of the unstable and stable manifolds of the saddle points of the period-5 orbit, found about the source on the left-hand side of the map, for $\alpha = 5.5$–5.9. Figures (c) and (e) also contain the right-hand sides of the Poincaré map as this shows the attraction of the stable manifolds of the periodic saddle orbit on the left-hand side of the map to the repelling invariant circle on the right-hand side.

get smaller with increased α and interacts with other period orbits it comes across in the same manner as described above (see Fig. 6(a)–(e)) which show the passage of the invariant circle though a period-4 chain.

As is to be expected, the mechanism described is almost identical to that described by Arrowsmith et al. [34,35] for an invariant circle moving through the Bogdanov map. In our case, however, instead of heteroclinic tangles when the invariant circle interacts with the unstable and stable manifolds of the saddles of the periodic orbit there are smooth heteroclinic connections, or at least the lobes of the tangle are so small as to be unobservable. This is

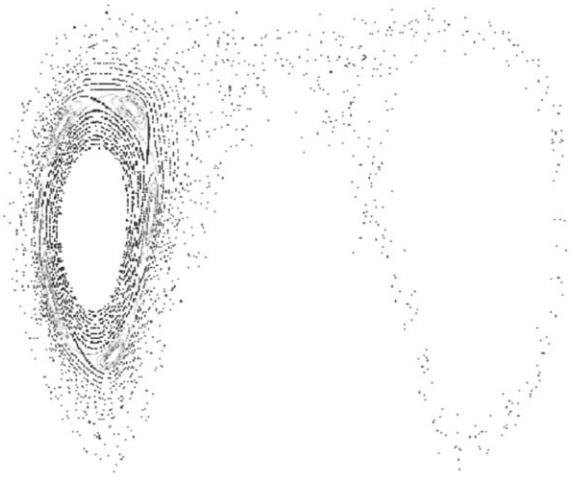

(c) $\alpha = 5.65$.

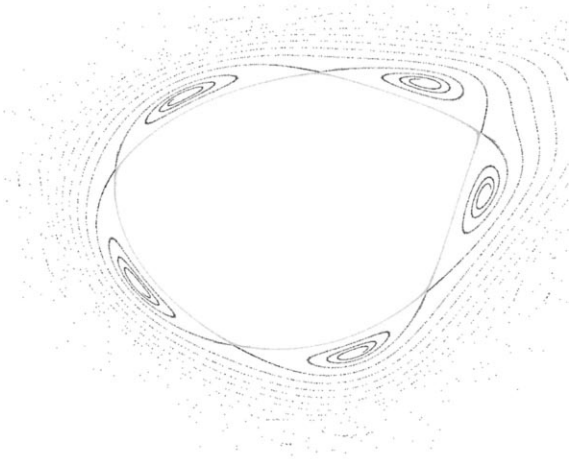

(d) $\alpha = 5.741$.

Fig. 5. (*Continued*).

slightly unexpected, though it shows that the presence and strength of the attracting or repelling periodic orbits and invariant circles locally control the system to such an extent to prevent tangles. This would restrict the behaviour to being non-chaotic in these regions.

The behaviour of the invariant circle and its interaction with the Birkhoff periodic orbits is important to the global and local transport. As we shall see in the next section, this behaviour has a major effect on the ultimate fate of a patch of material.

5. Lobes, definitions and dynamics

The global transport is highly dependent upon the relative position of invariant circles and the nature of both the elliptical/focus/saddle fixed points and of the tangle of the fixed saddle point. In terms of our model this means

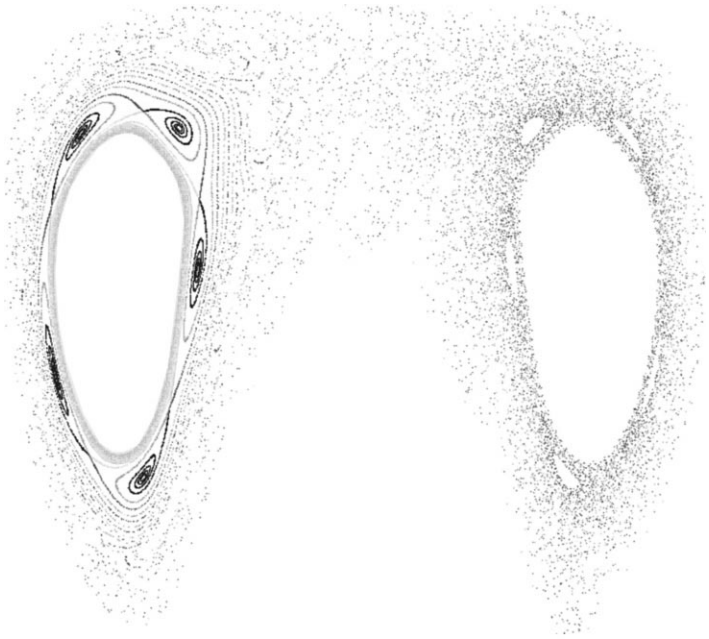

(e) $\alpha = 5.9$.

Fig. 5. (*Continued*).

the ultimate fate of the particles is highly sensitive on α. This will have important consequences for both two- and three-dimensional mappings, and their fluid applications.

In this section we present lobe diagrams, their definitions, and dynamics. We extend the work in [1–3,17–19] to enable us to study transport in non-area-preserving maps of fluid flows where the stable and unstable manifolds do not tangle. The development is based mostly on the simplified lobe diagrams seen in Figs. 7–9 (see [10,11] for work on slightly dissipative forced systems).

We let $L_{i,j}(n)$ be the lobe which maps from region R_i to region R_j under n iterations of the mapping (see Figs. 7–9). Under the action of the map $L_{i,j}(n)$ maps to $L_{i,j}(n-1)$. If the mapping preserves area then the areas in $L_{i,j}(n)$ and $L_{i,j}(n-1)$ must be equal. For non-area-preserving mappings this is not the case. Also for non-area-preserving mappings the area leaving region R_j and the area entering region R_j need not necessarily be equal (i.e. area in $L_{i,j}(n) \neq$ the area in $L_{j,i}(n)$). This, along with the fact that in these non-area-preserving systems there is the possibility of non-transverse intersections (i.e. tangential), and even the possibility of no intersection of the stable and unstable manifolds, is the main difference between these and time-periodic Hamiltonian systems. It has to be noted that in these cases we no longer have what can be termed a turnstile lobe, and so we have to understand the transport in a slightly different manner.

If we look at Figs. 7–9 we can understand the effect of the homoclinic bifurcation on the global dynamics and transport. For the case before the homoclinic tangency (Fig 7), where the unstable (W^{u}) and stable (W^{s}) manifolds cross transversely and lobes exist, we get transport into and out of the region R_j inside the tangle. When the unstable and stable manifolds of the saddle fixed point bifurcate in a homoclinic bifurcation to form a homoclinic tangency (Fig. 7) or a post-homoclinic tangency (Fig. 8) we lose the turnstile lobe and hence with it the possibility of a mutual exchange of material between regions R_i and R_j. This results in one way transport into or out of region R_j depending on whether the bifurcation is sub or supercritical. In other words whether the unstable manifold comes

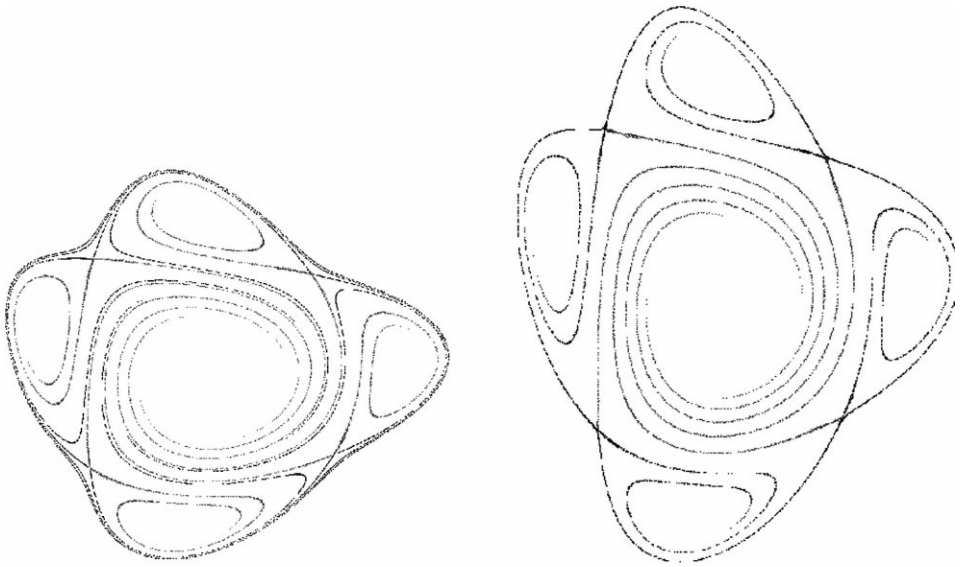

(a) $\alpha = 6.9$. (b) $\alpha = 6.91$.

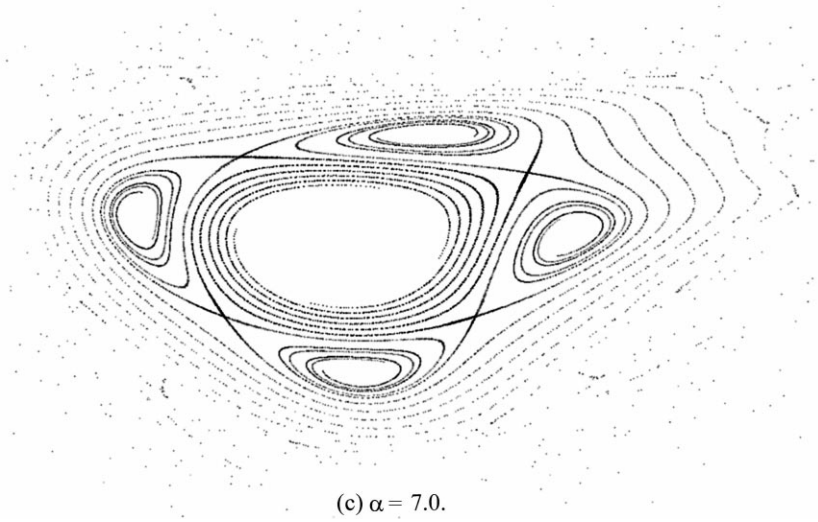

(c) $\alpha = 7.0$.

Fig. 6. The phase portrait of the unstable and stable manifolds of the saddle points of the period-4 orbit, found about the source on the left-hand side of the map, for $\alpha = 6.9$–7.3.

inside or outside of the stable manifold, respectively. Due to the loss of the tangle we have to consider how we define the two regions R_i and R_j. This is now a different system compared to the area-preserving system or even the non-area-preserving tangle system.

Our goal is to present the transport in the three (i.e. tangle, tangency and post-tangency) cases separately and then extend the idea of lobes and transport to cover all the three cases. We do this first for the case where we have a homoclinic tangle (see Fig. 7).

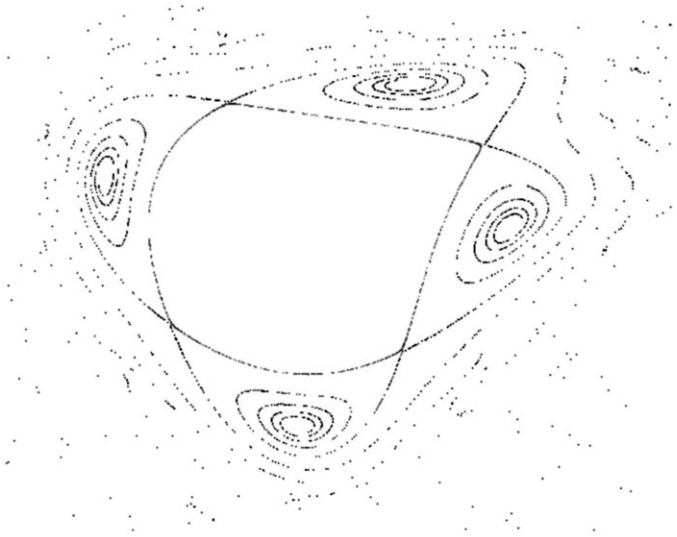

(d) $\alpha = 7.145$.

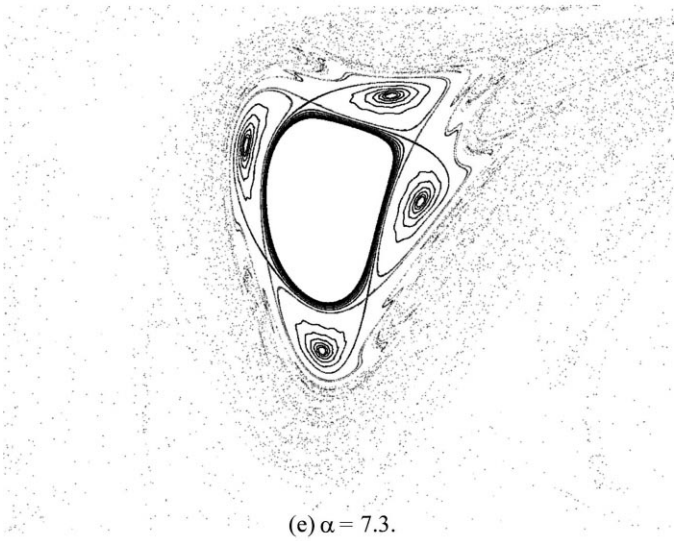

(e) $\alpha = 7.3$.

Fig. 6. (*Continued*).

5.1. The homoclinic tangle case

We start by recalling the homoclinic tangle case described in [17,19]. This is the case for which the original methods and definitions of Rom-Kedar and Wiggins [1] and Wiggins [2], were developed, as it occurs generically in area-preserving maps. Fig. 7 shows the unstable $W^{\mathrm{u}}(p_i)$ and stable $W^{\mathrm{s}}(p_i)$ manifolds of a fixed point p_i.

Suppose $q \in W^{\mathrm{s}}(p_i) \cap W^{\mathrm{u}}(p_i)$ and let $S[p_i, q]$ denote the segment of $W^{\mathrm{s}}(p_i)$ with end points p_i and q and $U[p_i, q]$ denote the segment of $W^{\mathrm{u}}(p_i)$ with endpoints p_i and q. Then q is called a *primary intersection point* if $S[p_i, q]$ intersects $U[p_i, q]$ only at the points p_i and q.

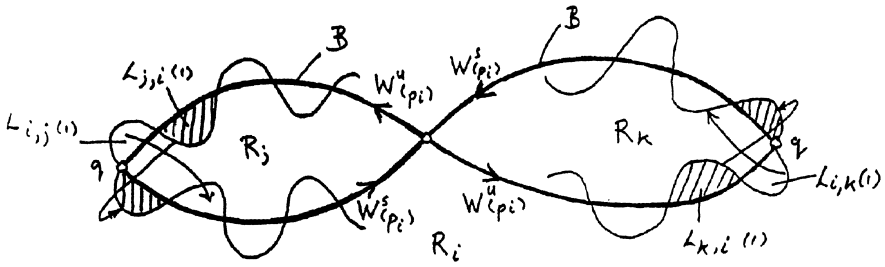

Fig. 7. The simplified lobe diagram for the homoclinic tangle of the unstable $W^{\mathrm{u}}(p_i)$ and stable manifolds of a saddle fixed point p_i.

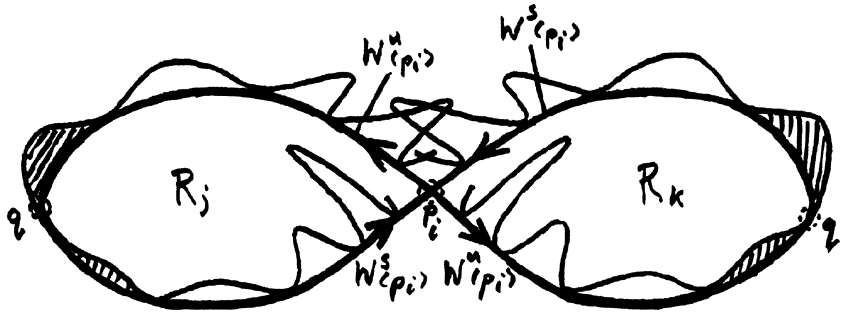

Fig. 8. The simplified lobe diagram for the homoclinic tangency of the unstable $W^{\mathrm{u}}(p_i)$ and stable manifolds of a saddle fixed point p_i.

Let $q_0, q_1 \in W^{\mathrm{s}}(p_i) \cap W^{\mathrm{u}}(p_i)$ be two adjacent primary intersection points, i.e. there are no other primary intersection points on $U[q_0, q_1]$ and $S[q_0, q_1]$, the segments of $W^{\mathrm{u}}(p_i)$ and $W^{\mathrm{s}}(p_i)$ connecting q_0 and q_1. Then the region interior to $U[q_0, q_1] \cup S[q_0, q_1]$ is referred to as a *lobe*. Remember that q_1 is not an iterate of q_0.

If $W^{\mathrm{s}}(p_i)$ and $W^{\mathrm{u}}(p_i)$ intersect at the primary intersection point q, the partial barrier B can be defined as $B = S[p_i, q] \cup U[p_i, q]$. The region interior to $S[p_i, q] \cup U[p_i, q]$ is referred to as R_j, while R_i refers to that which is exterior, with the *turnstile lobe* $L_{i,j}(1)$ and $L_{j,i}(1)$ being the lobes which map from region R_i to region R_j and region R_j to region R_i, respectively, under one iteration of the mapping. The general case is the lobe $L_{i,j}(n)$, which maps from region R_i to region R_j under n iterations of the mapping.

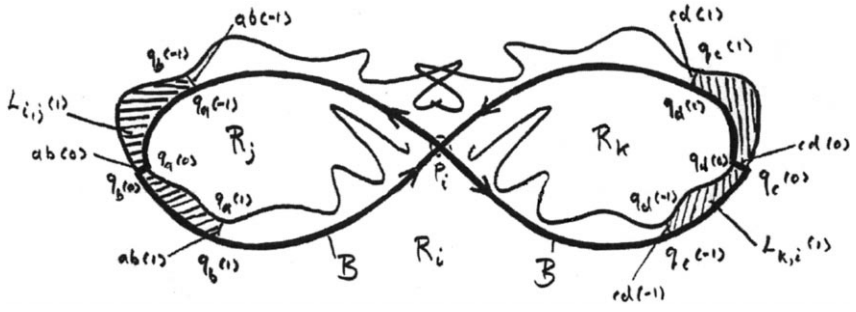

Fig. 9. The simplified lobe diagram for the post-homoclinic tangency of the unstable and stable manifolds of a saddle fixed point p_i.

5.2. The homoclinic tangency case

We now extend the use of the above definitions to the case where $W^{\mathrm{u}}(p_i)$ and $W^{\mathrm{s}}(p_i)$ meet tangentially (see Fig. 8). It can be seen that we no longer have a turnstile lobe. Either the lobe $L_{i,j}(1)$ or $L_{j,i}(1)$ has shrunk to zero. The lobe which shrinks to zero depends on whether the bifurcation is sub- or super-critical (i.e. if the stable manifold comes inside the unstable one then $L_{i,j}$ shrinks to zero, but if the opposite happens, W^{u} comes inside W^{s}, then $L_{j,i}$ shrinks to zero (see the right and left halves of Fig. 8, respectively.) Also we no longer have a primary intersection point, as the two manifolds do not cross. We do though have what we term a *primary tangential point*.

Suppose $q \in W^{\mathrm{s}}(p_i) \cap W^{\mathrm{u}}(p_i)$ and let $S[p_i, q]$ denote the segment of $W^{\mathrm{s}}(p_i)$ with end points p_i and q and $U[p_i, q]$ denote the segment of $W^{\mathrm{u}}(p_i)$ with endpoints p_i and q. Then we define q to be a *primary tangential point* if $S[p_i, q]$ touches tangentially $U[p_i, q]$ only at the point q. We now use this to redefine a lobe.

Let $q_0, q_0(1) \in W^{\mathrm{s}}(p_i) \cap W^{\mathrm{u}}(p_i)$ be two adjacent primary tangential points, i.e. there are no other primary tangential points on $U[q_0, q_0(1)]$ and $S[q_0, q_0(1)]$, the segments of $W^{\mathrm{u}}(p_i)$ and $W^{\mathrm{s}}(p_i)$ connecting q_0 and $q_0(1)$. $q_0(1)$ is the first positive iterate of q_0. We then define the region interior to $U[q_0, q_0(1)] \cup S[q_0, q_0(1)]$ to be a *lobe*. The lobe $L_{i,j}(n)$ is still defined in the same way as in the tangle case.

We now define the partial barrier as $B = S[p_i, q] \cup U[p_i, q]$, where $W^{\mathrm{s}}(p_i)$ and $W^{\mathrm{u}}(p_i)$ touch at a primary tangential point q. We refer to the region interior to $U[p_i, q] \cup S[p_i, q]$ as R_j.

5.3. The post-tangency case

For the post-tangency case where the two manifolds W^{s} and W^{u} no longer touch we have to artificially connect them so as to produce two regions R_j and R_i and hence lobes (see Fig. 9).

We connect the two manifolds by an arbitrary line $ab(0)$, connecting the arbitrary points $q_a(0) \in W^{\mathrm{u}}(p_i)$ and $q_b(0) \in W^{\mathrm{s}}(p_i)$. We then define the barrier $B = S[p_i, q_b(0)] \cup U[p_i, q_a(0)] \cup ab(0)$, and we refer to the region interior to B as R_j.

We define the lobe as the region interior to $U[q_a(n), q_a(n+1)] \cup S[q_b(n), q_b(n+1)] \cup ab(n) \cup ab(n+1)$, where $q_a(n+1)$, $q_b(n+1)$ and $ab(n+1)$ are the first positive iterates of $q_a(n)$, $q_b(n)$ and $ab(n)$, respectively. The lobe $L_{i,j}(n)$ is still defined in the same way as in the tangle case.

Though these extensions we have developed are very simple, they now allow us to understand transport in a larger class of non-area-preserving systems using lobe diagrams. It also has to be noted that the extension to the heteroclinic case is straightforward, and will be shown in the next section (see Figs. 10 and 15).

The area of these lobes have to be found numerically. The variational principles method [3] or a Melnikov type method [4] are not applicable. This is due, respectively, to the facts that the map does not preserve area, and that the problem cannot be thought of in the terms of a perturbation, as in our practical applications we are interested in too large a value of α. It should be noted, however, that if we could consider our model in terms of a perturbation then Hinenzon and Rom-Kedar [10,11] show that Melnikov theory can be used to compute flux even when there is no intersection of the stable and unstable manifolds (i.e. even when there is no tangle).

6. Transport associated with periodic orbits

We can apply the above definitions to the case of finding the transport across barriers formed from segments of the stable and unstable manifolds of the saddle fixed point seen in our system. We now apply it, however, to the periodic orbits to highlight the importance to transport of the bifurcations undergone by the unstable and stable manifolds of the periodic saddle points, as they come in and out of resonance with the invariant circle.

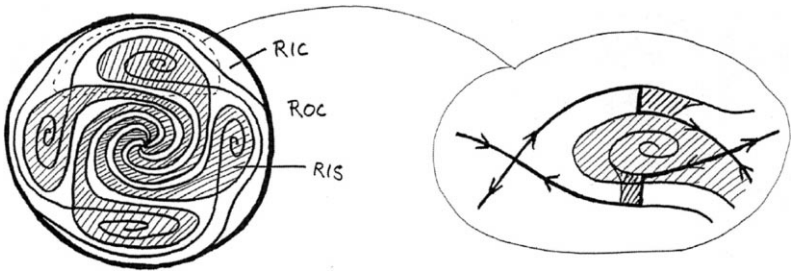

Fig. 10. The simplified lobe diagram, corresponding to Fig. 6(a), for the period-4 island chain, and the invariant circle. Case 1, where the invariant circle is on the outside of the periodic island chain, and not in resonance with it.

If we look at the unstable and stable manifolds of the periodic orbits, we see that they look similar to how they would in a flow. This is counterintuitive as we have a map and would generically expect to see tangles. As can be seen from Figs. 5 and 6 tangles do not occur, or they are so small that to all intense and purposes they do not exist. We suggested earlier that the lack of heteroclinic tangles for these periodic orbits is a product of the strength of nearby attractors and repellers. It can been seen that they can dominate the dynamics to such an extent so as to produce non-chaotic regions. The possibility of the generation of Smale horseshoes via the tangle of the manifolds is lost.

We look at an example of the transport through barriers formed from stable and unstable manifolds of period-4 saddle Birkhoff periodic chains, as the invariant circle comes in and out of resonance. To do so we schematically redraw Fig. 6(a)–(e) in order to exhibit the general transport properties more clearly (see Figs. 10–14). Although we have greatly simplified these figures the general transport mechanisms remain the same. We now use these simplified figures to illustrate how the ultimate fate of a particle or patch of material can be sensitively dependent on α, especially in the presence of an invariant circle. If we look at Fig. 10 we can define regions depending on where the material came from. R_o is the outside of the invariant circle (or periodic chain, when the invariant circle is in resonance), and R_i is the inside. As can also be seen, these regions need to be divided yet again depending on where the contents end up. For example, if we look at Fig. 14, we see that we need to split the region outside the invariant circle into the two regions R_{os} and R_{oc}, where points in R_{os} are attracted to the periodic sink, and points in R_{oc} are attracted to the invariant circle. We can now split the phase space into a maximum of four different regions, or basins of attraction.

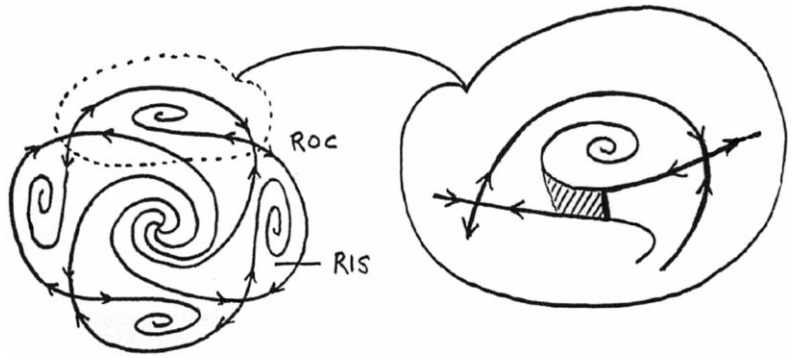

Fig. 11. The simplified lobe diagram, corresponding to Fig. 6(b), for the period-4 island chain, and the invariant circle. Case 2, where the invariant circle is now absorbed into the upper unstable and stable manifolds of the saddle points of the island chain.

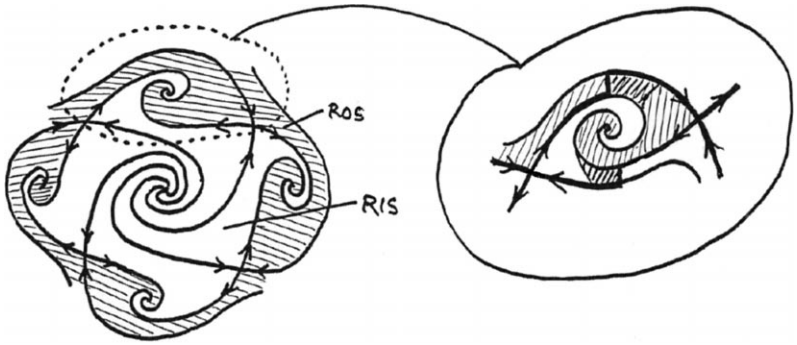

Fig. 12. The simplified lobe diagram, corresponding to Fig. 6(c), for the period-4 island chain, and the invariant circle. Case 3, where the invariant circle has disappeared and is in resonance with the periodic island chain.

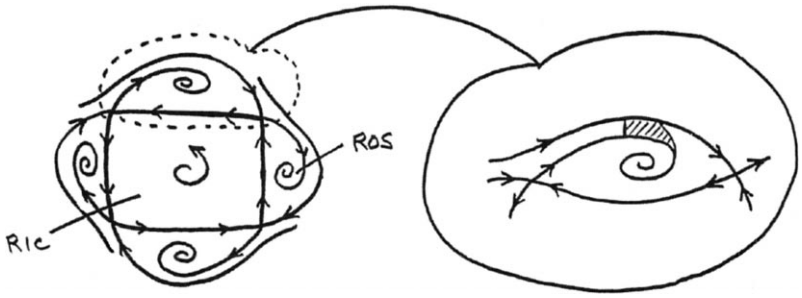

Fig. 13. The simplified lobe diagram, corresponding to Fig. 6(d), for the period-4 island chain, and the invariant circle. Case 4, where the invariant circle is now absorbed into the lower unstable and stable manifolds of the saddle points of the island chain.

The general transport properties of the Figs. 10–14 can be related to the presence (or lack) of the four possible basins of attraction (R_{ic}, R_{is}, R_{oc}, and R_{os}). The existence of a basin of attraction is dependent upon the bifurcation undergone by the unstable and stable manifolds of the periodic chain. This therefore results in a sensitive dependence of the transport in this area to the parameter α. With the invariant circle on the outside of the periodic chain (Fig. 10), the material on the inside can be in either of the two basins, R_{ic} and R_{is}. Material can therefore pass through the periodic chain, and be attracted to the invariant circle. All the material from outside the chain is also attracted to the

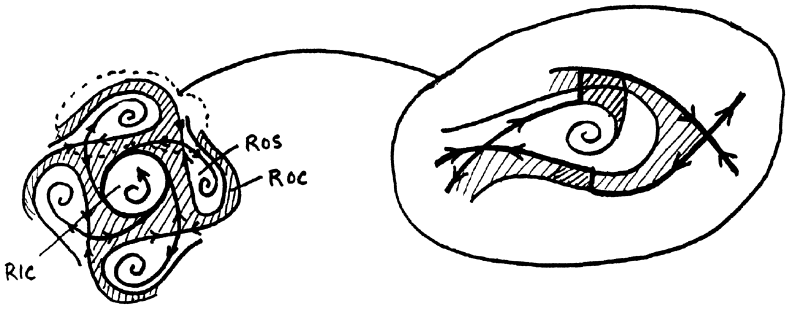

Fig. 14. The simplified lobe diagram, corresponding to Fig. 6(e), for the period-4 island chain, and the invariant circle. Case 5, where the invariant circle is on the inside of the periodic island chain, and not in resonance with it.

invariant circle, via the basin R_{oc}. If we now increase α (see Fig. 11), the basin R_{ic} shrinks to zero. It ceases to exist, when the outer manifolds of the saddle join in a heteroclinic connection and the invariant circle comes in resonance with the island chain. All the material on the inside therefore exists in the basin R_{is}. All the material on the outside still exists in the basin R_{oc}. A further increase in α (Fig. 12) has no effect on the fate of the material on the inside, it still exists entirely in the basin R_{is} and is therefore fully attracted into the periodic sink. However, due to the loss of the invariant circle, the basin R_{oc} no longer exists, and hence all the material on the outside exists in the basin R_{os}, and is attracted to the periodic sink. The fate of everything for this value of α therefore is to be attracted to the periodic sink. Further increases in α (Fig. 13) now lead to the invariant circle forming a heteroclinic connection with the inner unstable and stable manifolds of the saddle, and hence a barrier. This results in the loss of the basin R_{is} and all the material existing in R_{ic}, and hence being attracted to the barrier. On the outside, however, there is no change and all the material still exists in the basin R_{os}. Finally as the value of α is increased to such an extent that the invariant circle is no longer in resonance with the periodic island chain, and the heteroclinic connection is broken, there exists the possibility of transport through the island chain from the outside (see Fig. 14). Both basins of attraction R_{os} and R_{oc} now exist, and there remains only the one basin, R_{ic} on the inside.

We can now calculate the transport into sinks or through the periodic chains to invariant circles (see the blown up segments of Figs. 10–14). We create the lobes in a similar way to the post-tangency case described in Section 5.3. We connect the outer and inner unstable and stable manifolds, respectively, of the adjacent periodic saddle points, p_i and p_{i+1} (see Fig. 15) .

We can now define the barrier B as described in Fig. 15. We connect the two outer and inner unstable and stable manifolds by the arbitrary curves $ab(0)$, and $cd(0)$ connecting the arbitrary points $q_a(i) \in W^u(p_i)$ and $q_b(i) \in W^s(p_{i+1})$, and $q_c(i) \in W^u(p_{i+1})$ and $q_d(i) \in W^s(p_i)$, respectively. We then define the barrier

$$B = \sum_{i=0}^{i=n-1} (U[p_i, q_a(i)] \cup S[p_{i+1}, q_b(i)] \cup ab(i) \cup U[p_{i+1}, q_c(i)] \cup S[p_i, q_d(i)] \cup cd(i)) \tag{22}$$

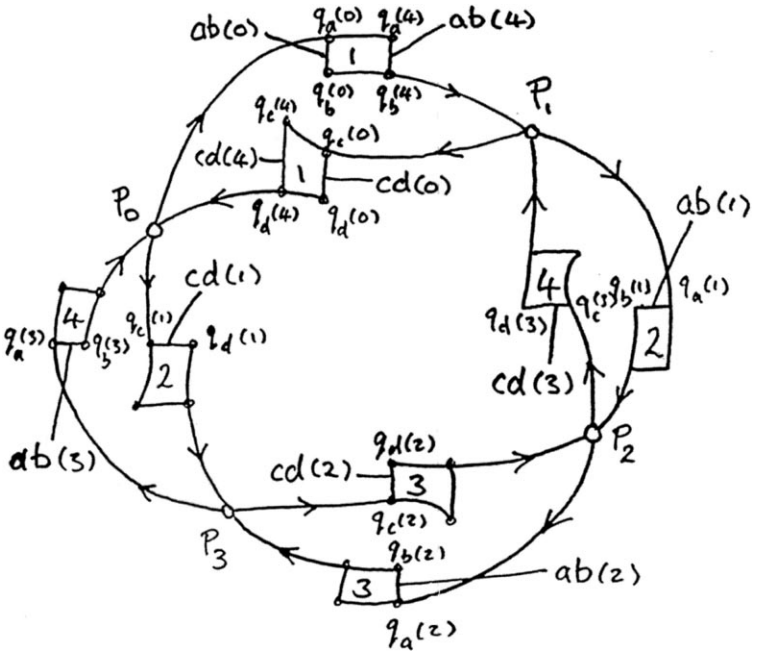

Fig. 15. The simplified lobe diagram showing the construction of the barrier B for case 1 (see Fig. 10a).

for a period-n chain. As before we refer to the region interior to B as R_j. The *lobe* can now be defined in a similar manner. We define a *lobe* for a periodic orbit as the region interior to

$$U[q_a(m), q_a(m+n)] \cup S[q_b(m), q_b(m+n)] \cup ab(mn) \cup ab(m+n), \tag{23}$$

where $q_a(m+n)$, $q_b(m+n)$ and $ab(m+n)$ are the nth positive iterates of $a(m)$, $b(m)$ and $ab(m)$, respectively. The region interior to $U[q_c(m), q_c(m+n)] \cup S[q_d(m), q_d(m+n)] \cup cd(m) \cup cd(m+n)$ is also a lobe, where $c(m+n)$, $d(m+n)$ and $cd(m+n)$ are the nth positive iterates of $c(m)$, $d(m)$ and $cd(m)$, respectively. The lobe $L_{i,j}(n)$ is still defined in the same way as in Section 5.

Fig. 15 corresponds to the case $m = 0, n = 4$. This corresponds to the formation of a lobe and the barrier for $\alpha = 6.9$ (see Figs. 6(a) and 10). Using this approach we can now work out the transport through periodic chains.

If we now take a closer look at the lobes of Figs. 10–14, we see a range of dynamics. In Fig. 10 we see that the top lobe exists in the basin of the invariant circle and hence must have crossed the barrier B to be attracted to the invariant circle. The bottom lobe is split into two, with part being in the basin of the sink and part in the basin of the invariant circle. As we increase α (Fig. 11), we lose the top lobe altogether, due to a heteroclinic connection. The bottom lobe in Fig. 11 is now no longer split into two and hence it is all in the basin of the sink. As α is increased further, we no longer have a heteroclinic connection on the top, see Fig. 12, and hence we have a lobe which is only in the basin of the sink. On the bottom we also have a lobe which is only attracted to the same sink. If we now look at Fig. 13, we can now see by increasing α we see a similar figure to Fig. 11, though this time the heteroclinic connection is on the bottom. The only material passing the barrier B is in the basin of the sink and comes from outside the invariant circle. As α is increased, we can now see a similarity between Figs. 10 and 14. The invariant circle is now on the inside of the periodic chain and therefore it is the top lobe which is split into two. Part of this lobe is attracted to the sink and part to the invariant circle, while the entire bottom lobe is attracted to the invariant circle. It can be seen in both these cases 10 and 14 that when the lobe is split into two, part of the split lobe is made up of parts of the pre-images of the other lobe.

We now consider what happens to a blob of material as it interacts with a source or sink on a two-dimensional invariant manifold corresponding to a bounding surface of a three- or (3+1)-dimensional volume preserving flow. This is important as it highlights the three-dimensional nature of sources and sinks and models the process of up-welling and down-welling. (For practical examples of such behaviour in tidal or estuarine flows see, [45–51].) When in the basin of attraction of a sink, the area of a blob obviously shrinks to zero in the $t = \infty$ limit, as it is attracted to the sink. This is same sort of dynamics as we see when material is attracted into a vortex. The material is sucked into its centre, and then out of the section, or surface, to another part of the fluid, this is what we call down-welling. If the patch was in the basin of attraction of a source we would see a patch of material appear on the surface and increase in size. This can be thought of as up-welling, where the dynamics of the fluid is up onto its surface, and we see the appearance of material from below the surface. Also a blob of material can be attracted to the invariant circle. Given enough time and a sufficiently stable invariant circle the blob will form a ring, whose boundary is the invariant circle, whose thickness will shrink to zero. It has to be remembered, however, that in practical applications, we will only see the invariant circle as a barrier for its more stable states (i.e. when it is not in resonance with a periodic chain).

7. Implications for fluid flows

In this section we look at the implications for clouds of pollution in a partially stratified estuary. We also discuss the effect of the coupling α on our recommendations for the discharge of pollution into the estuarine environment. In [17–19] we discussed this, in the context of an uncoupled three-dimensional time-periodic model.

As discussed in [17–19], if we are to discharge pollution into an estuary we have to understand the mixing properties of the particular region to which we discharge. Not only this but we also have to have an understanding how long the pollutant will remain in the region into which it has been discharged and where it will go once it leaves. We can optimise these three considerations and discharge at a site in which the combination of mixing and exit considerations are optimal. For example we would not want to discharge pollution in a region where the drift of the pollution would be back upstream, possibly towards the town it was discharged from. Neither would we want to discharge pollution into a region where the mixing was poor, or even worse a region where the pollution was sucked into one of the attracting regions we discussed. The best region would be a region were the diffusion was highest, such as the region local to the turnstile lobe of the hyperbolic fixed point, or some other chaotic region.

If we look at the lobe diagrams (for example Figs. 5(b), (e) and 6(e)) we see that the area of the turnstile lobe or in other words the diffusion associated with the periodic chains could only be very small. (As in [17–19] we use the fact that the area of the turnstile lobe is a local measure of diffusion.) If we take $\alpha = 5.9$ for example (see Fig. 5), we find that the diffusion associated with the lobes of the periodic chain are 4 or 5 orders of magnitude less than that due to turbulent diffusion. In [18,19], we assumed that when the turnstile lobe is very small then the diffusion in such a region is due mainly to turbulent diffusion and the region is essentially a trapping region, with the diffusion due to the template being insignificant. We make the same assumption here. Such trapping regions we claim would be responsible for some of the patchiness seen in clouds of pollution (see [52–54] for field observations of tracer experiments in various coastal regions, including estuaries, which show the existence of multiple maxima (i.e. patchiness) in dispersing clouds). We then expect to see patchiness corresponding to fuzzy or diffuse versions of our attracting periodic chains in the vertical cross-section of the estuary for values of the turbulent diffusion sufficiently small. These observations apply for values of α for which reasonably sized structures exist in the map of the template to the estuarine flow (e.g. for $\alpha = 5.5$). However, as we discussed earlier, the presence of the basin of attraction of these chains is highly sensitive on the coupling parameter α. Therefore we are only likely to see the more structurally stable phenomena, such as the invariant circle when it is not in resonance.

We now look at the stability of a fixed or periodic point found on the sea end boundary of the estuary and consider the (unstable or stable) manifold orthogonal to this boundary. We can see from the stability of this manifold whether the pollution near the sea end barrier will drift back into the estuary or whether pollution from elsewhere in the estuary could move into this cross-section. To preserve volume, regions of attraction in one plane must be regions of repulsion in another and vice versa. Therefore, any regions of attraction found on the sea end boundary will attract material into them in the vertical plane while at the same time repelling it from the surface back into the estuary. The converse is obviously true for regions of repulsion. This time material could be attracted towards the sea end barrier while at the same time being repelled when on the sea end boundary.

As described in Section 4 we find as we increase the strength of the coupling (i.e. the size of the parameter α), the size of the ordered regions within the cross-section of the fluid reduce, as the two invariant circles shrink. Simultaneously, the size of the lobes of the tangle of the stable and unstable manifolds of the hyperbolic fixed point increase. This results in the diffusion rates associated with the tangles of the hyperbolic fixed point found in the template of the estuarine flow increasing and therefore contributing more to the diffusion in the estuarine flow. (It can be shown that for $\alpha = 0$ (see [17–19]) the diffusion due to the turnstile lobe associated with the tangles of the unstable and stable manifolds of the hyperbolic fixed point is three orders of magnitude less than that due to turbulence, while for $\alpha = 10$ (see Fig. 2) the two diffusivities are of similar orders of magnitude.) For a strongly coupled flow (e.g. $\alpha = 10$), structures such as the periodic ones we observed for weak coupling are not found and the average mixing would as a result be much improved. The dynamics and transport in the estuarine flow, however, would still be able to be understood via the unstable and stable manifolds of fixed and periodic orbits in the flow. Such manifolds play an important role as the transport or diffusion associated their resultant turnstile lobe is closer to that due to turbulent diffusion.

We conclude with the obvious fact that if we want to discharge pollution into our estuary, then it would be best done if the values of α were high. Such a policy would of course be impractical as it would mean we could discharge only during the winter months for example when the estuary was in flood and the magnitude of the X-directional velocity and hence the coupling were increased (see Eq. (1), where it can be seen that $\mathcal{U}_f$ is an increasing function of α). This observation leads to the useful fact that more pollutant could be discharged during times of flood, with the converse also being true, that less should be discharged during times of drought. Although this is a somewhat obvious comment it shows us that common sense and engineeringly useful results can still be obtained from very simple low-dimensional models of estuarine flows. However, the attracting vortex and ring like structures that we predict occur for certain small values of α, and sufficiently small values of the turbulent diffusion, are much more unexpected and in many ways more interesting. This is due to their potential for causing patches of high concentration and hence a severe environmental impact if a cloud of pollution was to interact with them. Also, the presence of regions where the drift of pollution would be back upstream against the flow of the estuary is unexpected and important especially when considering where to discharge pollution. As we said earlier the discharge of pollution from a town or city into such a region would be highly undesirable, especially considering the fact that they correspond to sinks (i.e. regions of attraction on our two-dimensional invariant manifold) and hence would form tubes of high concentration from which the diffusion would be due only to the effects of turbulence. Finally, it should also be noted when considering the position of a possible out-fall site that (as was shown in [18,19]) regions where the mixing is best (i.e. near the bed of the estuary where the velocity gradients are largest, due to the non-slip boundary conditions) are regions where the pollution would remain longest (due essentially to the close proximity of zero velocities at the boundaries). This means that even though the mixing is good in such regions they remain undesirable for a site from which pollution is discharged and hence a compromise has to be reached between the mixing properties and the length of time for which pollution remains in a region (see [18,19] for a more complete discussion regarding exit times, mixing and the optimal co-ordinates for the release of pollution into an estuarine flow).

8. Summary

We have extended the theory of transport in a fluid via lobe diagrams to the case where the unstable and stable manifolds of saddle points in a map no longer tangle (i.e. they meet tangentially or not at all). Such cases occur in non-area-preserving two-dimensional maps which in turn can be found to occur generically on the bounding surfaces of (3+1)-dimensional fluid flows. The extension we present is important as in practice the flow on such surfaces is usually modelled by an area-preserving system which is often unsatisfactory. Obviously, such systems cannot contain attractors (i.e. sinks and sources) and therefore they fail to model major features of the flow, such as the transport into a vortex, very well at all. We have applied these ideas to a model of the flow on one of the bounding surfaces of an estuary. This model is an extension of the (3+1)-dimensional uncoupled system presented in [17–19], to a (3+1)-dimensional fully-coupled time-periodic flow.

We present the three possible states which the unstable and stable manifolds of saddle points in these non-area-preserving maps may take as they undergo a homoclinic bifurcation. Firstly, there is the case where the manifolds meet transversely, tangle and hence form a turnstile lobe; secondly, where the manifolds meet tangentially, there is no tangle, and hence there is also no turnstile lobe, though there are lobes; and finally, where the manifolds do not touch at all, and hence there are no lobes (we have to add extra curves to obtain lobes) and no tangle.

Fig. 6a–e and their simplified versions Figs. 7–14 highlight the importance of the attracting and repelling invariant circles often found in such maps. As we can see, the ultimate fate, and even the degree of mixing undergone by a patch of material, is highly sensitive to both the position and presence of such circles. We see that over a small parameter range the form taken by the invariant circle can vary greatly depending on its relationship with resonant and non-resonant Birkhoff periodic chains. This is important as some of these forms are more stable than others. By

this we mean the invariant circle is much more stable when not in resonance, as when it is in resonance its presence is sensitively dependent on α. This is important in practice, as in practical applications we are only likely to see the existence of the invariant circle as a barrier, if it is in its more stable state (i.e. not when it is in resonance). We would, however, feel its effect on a periodic chain. We would only see these in practice, as a vortex in a flow, when the invariant circle is in resonance with the periodic chain. This is because the basin of attraction of a resonant island chain is far bigger than when it is not in resonance. The case where the invariant circle is in resonance with the periodic orbit and does not exist (Figs. 5c and 6c) and is also a structurally stable state. For our model, however, it is much less stable (i.e. exists for a smaller interval of α) than the case where the invariant circle is no longer in resonance (Figs. 5e and 6a).

Both the structurally stable features mentioned above are most likely to be seen in the full estuarine flow for low values of α, as this is when they are largest in size. As α is increased the size of these ordered regions in the flow decreases and hence as a result the mixing improves. Due to $\mathcal{U}_{\mathrm{f}}$ being an increasing function of α, large values of α correspond to large values of $\mathcal{U}_{\mathrm{f}}$ (i.e. flood conditions). Therefore, the observation regarding improved mixing with increasing α supports the standard practice of releasing more pollution in times of flood and less in times of drought.

We can also see that the strength of the attraction of the invariant circle and the sinks in the periodic chains can be such that they prevent the unstable and stable manifolds of the saddle points tangling, or at least reduce the size of the lobes resulting from such a tangle to such an extent so as to make them unobservable. This has important consequences for the mixing and discharge of pollution in our flow, as it provides a mechanism to create regions of very high concentration (see Figs. 10–14). In these figures, we have regions where there is no exchange of material between adjacent regions. Hence we have a mechanism for creating regions of very high or low concentration, similar to what is observed practically (see for example [52–54]) as patches of high or low concentration in clouds of pollution. Such regions are of major importance, as they are one of the key factors in determining the polluting capabilities of a cloud of pollution.

Insights into how to understand and model the transport in three-dimensional maps or (3+1)-dimensional time-periodic flows can also be gained from what we have presented here. We now have an understanding of the flow and the behaviour of the unstable and stable manifolds of the saddle points on both the river, $X = 0$ [17,19], and sea, $X = 1$, ends of our model. An understanding of bifurcation and transport on these end surfaces goes some way towards a similar understanding of the full three-dimensional map or (3+1)-dimensional flow.

We now have a simple "off the shelf" extension to the transport theory of Rom-Kedar and Wiggins [1] and Wiggins [2] which is easy to apply and allows us to understand the transport for a much larger class of non-area-preserving maps than just those containing homoclinic and heteroclinic tangles, and hence provide better models for the transport on the surfaces of (3+1)-dimensional fluid flows.

Acknowledgements

I would like to thank Ron Smith and Cecil Scott for many helpful discussions. I would also like to acknowledge the support from my parents, grandparents, the Department of Mathematical Sciences, Loughborough University, UK (where this work was started) and EPSRC (who partially supported me while in Loughborough). Finally, I would also like to acknowledge the two referees for some helpful comments. This work was partially supported by the MIDIT centre at the Technical University of Denmark, and also by the Institute for Electronic Structure and Laser, Foundation for Research and Technology, Hellas (FORTH), through an EC TMR grant number HPRN-CT-1999-00163.

References

[1] V. Rom-Kedar, S. Wiggins, Transport in two-dimensional maps, Archive Rational Mech. Anal. 109 (3) (1990) 239–298.
[2] S. Wiggins, Chaotic Transport in Dynamical Systems, Interdisciplinary Applied Mathematics, Springer, Berlin, 1992.

[3] J.D. Meiss, Symplectic maps, variational principles and transport, Rev. Mod. Phys. 64 (1992) 795–848.
[4] S. Wiggins, Global Bifurcations and Chaos: Analytical Methods, Applied Mathematical Sciences, Springer, Berlin, 1988.
[5] G. Haller, Chaos Near Resonance, Applied Mathematical Sciences, Vol. 138, Springer, New York, 1999.
[6] J.H.E. Cartwright, M. Feingold, O. Piro, Chaotic advection in three-dimensional unsteady incompressible laminar flow, J. Fluid Mech. 316 (1996) 259–284.
[7] I. Mezic, On the integrability and perturbation of three-dimensional fluid flows with symmetry, J. Nonlinear Sci. 4 (1994) 157–194.
[8] I. Mezic, A. Leonard, S. Wiggins, Regular and chaotic particle motion near a helical vortex filament, Physica D 111 (1998) 179–201.
[9] G. Haller, I. Mezic, Reduction of three-dimensional, volume preserving flows with symmetry, Nonlinearity 11 (2) (1998) 319–339.
[10] A.L. Hinenzon, The homoclinic tangle of slightly dissipative, forced, two-dimensional systems, Masters Thesis, The Faculty of Mathematical Sciences, The Weizmann Institute of Science, 1995.
[11] A.L. Hinenzon, V. Rom-Kedar, Symmetry breaking perturbations and strange attractors, Phys. Rev. E 55 (5) (1997) 4964–4978.
[12] J.M. Ottino, The Kinematics of Mixing: Stretching, Chaos and Transport, Cambridge University Press, Cambridge, 1989.
[13] H.F. Aref, Stirring by chaotic advection, J. Fluid Mech. 143 (1984) 1–21.
[14] H.F. Aref (Guest Ed.), Chaos applied to fluid mixing, Chaos Solitons Fractals 4 (1994) 6.
[15] R. Pasmanter, Dynamical systems, deterministic chaos and dispersion in shallow tidal flows, in: Physical Processes in Estuaries, Springer, Heidelberg, 1988, pp. 42–52.
[16] H. Ridderinkhof, J.F.T. Zimmerman, Chaotic stirring in a tidal system, Science 258 (1986) 1107–1111.
[17] J.R. Stirling, Patches, patchiness and pollution, Preprint, 1999.
[18] J.R. Stirling, Chaotic advection, transport and patchiness in clouds of pollution in an estuarine flow, Preprint, 1999.
[19] J.R. Stirling, Painting pictures of turbulence: chaotic advection and transport in (3+1)-dimensional flows, Ph.D. Thesis, Department of Mathematical Sciences, Loughborough University, UK, 1998.
[20] S. Wiggins, Chaos in the dynamics generated by sequences of maps, with applications to chaotic advection in flows with aperiodic time dependancy, Z. Angew. Math. Phys. 50 (4) (1999) 585–616.
[21] N. Malhotra, S. Wiggins, Geometric structures, lobe dynamics, and Lagrangian transport in flows with aperiodic time dependancy, with applications to Rossby wave flow, J. Nonlinear Sci. 8 (4) (1998) 401–456.
[22] G. Haller, A.C. Poje, Finite time transport in aperiodic flows, Physica D 119 (1998) 352–380.
[23] A.C. Poje, G. Haller, The geometry and statistics of mixing in aperiodic flows, Phys. Fluids 11 (10) (1999) 2963–2968.
[24] G. Haller, A.C. Poje, Lagrangian transport and diffusion in two-dimensional aperiodic flows, Preprint, 1999.
[25] G. Haller, Finding invariant manifolds in two-dimensional velocity fields, Preprint, 1999.
[26] P.D. Miller, C.K.R.T. Jones, A.M. Rogerson, L.J. Pratt, Quantifying transport in numerically generated velocity fields, Physica D 110 (1997) 105–122.
[27] S. Balasuriya, C.K.R.T. Jones, B. Sandstede, Viscous perturbations of vorticity conserving flows and separatix splitting, Nonlinearity 11 (1) (1998) 44–77.
[28] R. Smith, Longitudinal dispersion of a buoyant contaminant in a shallow channel, J. Fluid Mech. 78 (4) (1976) 677–688.
[29] R. Smith, Buoyancy effects upon longitudinal dispersion in wide well-mixed estuaries, Philos. Trans. R. Soc. London 296 (1421) (1980) 467–496.
[30] C. Scott, A numerical study of the interaction of tidal oscillations and nonlinearities in an estuary, Est. Coast. Shelf Sci. 39 (1994) 477–496.
[31] J.R. West, J.S. Mangat, The determination and prediction of longitudinal dispersion coefficients in a narrow, shallow estuary, Est. Coast. Shelf Sci. 22 (1986) 161–181.
[32] I. Guymer, J.R. West, Field studies of the flow structure in a straight reach of the Conwy estuary, Est. Coast. Shelf Sci. 32 (1991) 581–596.
[33] R.A. Nunes, J.H. Simpson, Axial convergence in a well-mixed estuary, Est. Coast. Shelf Sci. 20 (1985) 637–649 .
[34] D. Arrowsmith, C. Place, An Introduction to Dynamical Systems, Cambridge University Press, Cambridge, 1990.
[35] D. Arrowsmith, J. Cartwright, A. Lansbury, C. Place, The Bogdanov map: bifurcations, mode locking and chaos in a dissipative system, Int. J. Bifurc. Chaos 3 (1993) 803–842.
[36] Y.A. Kuznetsov, Elements of Applied Bifurcation Theory, Springer, Berlin, 1995.
[37] D.G. Aronson, M.A. Chory, G.R. Hall, R.P. McGehee, Bifurcations from an invariant circle for two-parameter families of maps of the plane: a computer assisted study, Commun. Math. Phys. 83 (1982) 303–354.
[38] A.D. Morozov, A complete qualitative investigation of Duffing's equation, Differential Equations 12 (1976) 164–174.
[39] V.I. Arnol'd, Geometric Methods in the Theory of Ordinary Differential Equations, Springer, Berlin, 1983.
[40] B. Krauskopf, Bifurcation sequence at 1:4 resonance: an inventory, Nonlinearity 7 (3) (1994) 1073–1091.
[41] B. Krauskopf, The bifurcation set for the 1:4 resonance problem, Exp. Math. 3 (2) (1994) 107–128.
[42] B. Krauskopf, On the 1:4 resonance problem: analysis of the bifurcation set, Ph.D. Thesis, University of Groningen, the Netherlands.
[43] V.I. Arnol'd, Loss of stability of self-induced oscillations near resonance, and versal deformations of equivariant vector fields, Funct. Anal. i Priložen 11 (2) (1977) 1–10, 95 [English translation: Funct. Anal. Appl. 11 (2) (1977) 85–92].
[44] R.A. Abraham, C.D. Shaw, Dynamics —the Geometry of Behaviour, Part 4: Bifurcation Behaviour, Aerial Press Inc., Santa Cruz, CA, 1988.
[45] C.J.R. Garrett, R.H. Loucks, Upwelling along the Yarmouth Shore of Nova Scotia, J. Fish. Res. Bd. Can. 33 (1976) 116–117.
[46] R.D. Pingree, The formation of the shambles and other banks by tidal stirring of the seas, J. Mar. Biol. Assoc. UK 58 (1978) 211–226.

[47] E.J.L. Wolanski, M. Heron, Island wakes in shallow coastal waters, J. Geophys. Res. 89 (1984) 10553–10569.
[48] D.C. van Serden, J. Imberger, Effects of initial conditions and Ekman suction on tidal outflows from inlets, J. Geophys. Res. 95 (1990) 13373–13392.
[49] T.P. Signell, W.R. Geyer, Transient eddy formation around headlands, J. Geophys. Res. 91 (C2) (1991) 2651–2675.
[50] W.R. Geyer, Three-dimensional tidal flow around headlands, J. Geophys. Res. Oceans 98 (C1) (1993) 955–966.
[51] W.R. Geyer, R.P. Signell, A reassessment of the role of tidal dispersion in estuaries and bays, Estuaries 15 (2) (1992) 97–108.
[52] H. Postma, The distribution of temperature and salinity in the Wadden Sea, Tijdschr. K. Ned. Aardrijksk. Genoot. 67 (1950) 34–42.
[53] R. Dorrestein, On the distribution of salinity and of some other properties in the water of the Ems estuary, Verh. K. Ned. Geol.-Mijnd. Genoot. 19 (1960) 43–74.
[54] J.W. Talbot, G.A. Talbot, Diffusion in shallow seas and in English coastal and estuarine waters, Rapp. P. -v. Reun. Cons. Int. Explor. Mer. 167 (1974) 93–110.